

1  
2     **Ground-based Temperature and Humidity Profiling: Combining Active and**  
3         **Passive Remote Sensors**

4  
5  
6             David D. Turner<sup>1</sup> and Ulrich Löhnert<sup>2</sup>

7  
8             <sup>1</sup> NOAA / OAR / Global Systems Laboratory  
9             <sup>2</sup> University of Cologne / Institute of Geophysics and Meteorology

10  
11  
12             Submitted 31 August 2020  
13             [Updated on 15 Feb 2021](#)

14  
15             *Special Issue for the 11<sup>th</sup> International Symposium on Tropospheric Profiling in*  
16             *Atmospheric Measurement Technology*

17  
18  
19  
20  
21     Corresponding Author:  
22         Dr. David Turner  
23         NOAA Global Systems Laboratory  
24         325 Broadway, Boulder, CO 80305  
25         Voice: +1-303-497-6097  
26         Email: dave.turner@noaa.gov  
27  
28

29 **Abstract**

30 Thermodynamic profiles in the planetary boundary layer (PBL) are important observations for a  
31 range of atmospheric research and operational needs. These profiles can be retrieved from  
32 passively sensed spectral infrared (IR) or microwave (MW) radiance observations, or can be  
33 more directly measured by active remote sensors such as water vapor differential absorption  
34 lidars (DIALs). This paper explores the synergy of combining ground-based IR, MW, and DIAL  
35 observations using an optimal estimation retrieval framework, quantifying the reduction in the  
36 uncertainty in the retrieved profiles and the increase in information content as additional  
37 observations are added to IR-only and MW-only retrievals.

38  
39 This study uses ground-based observations collected during the Perdigao field campaign in  
40 central Portugal in 2017 and during the DIAL demonstration campaign at the Atmospheric  
41 Radiation Measurement Southern Great Plains site in 2017. The results show that the  
42 information content in both temperature and water vapor is higher for IR instrument relative to  
43 the MW instrument (thereby resulting in smaller uncertainties), and that the combined IR+MW  
44 retrieval is very similar to the IR-only retrieval below 1.5 km. However, including the partial  
45 profile of water vapor observed by the DIAL increases the information content in the combined  
46 IR+DIAL and MW+DIAL water vapor retrievals substantially, with the exact impact vertically  
47 depending on the characteristics of the DIAL instrument itself. Furthermore, there is slight  
48 increase in the information content in the retrieved temperature profile using the IR+DIAL  
49 relative to the IR-only; this was not observed in the MW+DIAL retrieval.

50  
51

52 **1. Introduction**

53 High temporal resolution thermodynamic profiles in the planetary boundary layer (PBL)  
54 are needed for a wide range of research and operational weather forecasting needs  
55 (Wulfmeyer et al. 2015). For example, the vertical distribution of water vapor and temperature  
56 changes markedly over the diurnal cycle, the passage of synoptic features such as frontal  
57 boundaries and dry lines can cause very rapid changes in the thermodynamic structure of the  
58 PBL, and the evolution of convective weather with evaporation-driven cold pools impacts both  
59 the temperature and humidity profiles and feeds back on the storm's evolution. Indeed, a large  
60 number of groups have called for improvements in the thermodynamic profiling in the PBL, and  
61 the establishment of ground-based networks to provide these datasets to the atmospheric  
62 science community (e.g., Dabberdt et al. 2005; NRC 2009).

63 Progress is being made, albeit perhaps slowly. There are a large number of case studies  
64 using PBL thermodynamic profiling systems to gain insight into how the convective properties  
65 of atmosphere changes (e.g., Feltz et al. 2003; Cimini et al. 2015; Bluestein et al. 2017; Toms et  
66 al. 2017; Mueller et al. 2017), analyses of long-time series to show the capability of these  
67 systems (Löhnert and Maier 2012; Wagner et al. 2008), and utility for improving short-term  
68 nowcasts and forecasts (e.g., Cimini 2011; Caumont et al. 2016; Hu et al. 2019; Coniglio 2019).

69 In Europe, there are a large number of microwave radiometers that are being  
70 characterized and assimilated (experimentally) into numerical weather prediction models  
71 (Cimini et al. 2018; De Angelis et al. 2017). Activities in the US have focused primarily on field  
72 campaigns, and the Plains Elevated Convection at Night (PECAN; Geerts et al. 2017) in  
73 particular, which deployed a small network of 6 infrared spectrometers in the central US. The  
74 PECAN observations are being used to study a range of atmospheric phenomena both  
75 observationally (e.g., Gasmick et al. 2018; Loveless et al. 2019) and via use in numerical weather  
76 prediction models (Johnson et al. 2018; Degelia et al. 2019).

77 However, these different ground-based remote sensors have generally not been  
78 collocated which makes evaluating the relative differences in the information content of the  
79 observations difficult. This paper takes advantage of two field campaigns where multiple  
80 ground-based remote sensing systems were collocated to evaluate the relative strengths and  
81 weaknesses of these different observations for thermodynamic profiling in the PBL. The two  
82 campaigns are Perdigao, which occurred in central Portugal in May-June of 2017 (Fernando et  
83 al. 2019), and a campaign at the ARM Southern Great Plains site (Sisterson et al. 2016) in May-  
84 June 2017 to compare a newly developed broadband differential absorption lidar for water  
85 vapor profiling with other instruments (Newsom et al. 2020).

86 **2. Instruments**

87 While there are many different instruments that could be included in this analysis, we  
88 will focus on four instruments that have been demonstrated to run operationally in unattended  
89 modes for weeks or longer, and either already are or will likely soon become commercially  
90 available. Two of these instruments are passive remote sensors (i.e., they do not transmit  
91 electromagnetic energy to the atmosphere) while two are active remote sensors.

92        **2.1. Microwave radiometer**

93        One type of passive thermodynamic profiler is a microwave radiometer (MWR). MWRs  
94        used for thermodynamic profiling typically have multiple channels along the high frequency  
95        side of the 22.2 GHz water vapor absorption line (i.e., from 22.2 to 31 GHz) and on the low  
96        frequency side of the 60 GHz oxygen absorption complex (i.e., from 51 to 60 GHz). Height  
97        dependent pressure broadening of the water vapor line allows the retrieval of a coarsely  
98        resolved water vapor profile, whereas temperature profile information is obtained from the  
99        frequency dependent optical depth. Generally speaking, the more transparent frequencies  
100        provide information through a deeper portion of the atmosphere and the optically thick  
101        channels provide information closer to the MWR. Oxygen is well mixed in the atmosphere and  
102        its concentration is known, thus the downwelling radiance observed in the channels that are  
103        primarily sensitive to oxygen can be used to infer the temperature profile. Water vapor  
104        concentration profiles can be determined from the channels that have sensitivity to water  
105        vapor after the temperature profile is known. However, there is some level of absorption due  
106        to oxygen in the 22-31 GHz range and water vapor in the 51-60 GHz range, so retrieval methods  
107        need to account for this ‘cross-talk’, and provide some estimate of the correlated errors in the  
108        retrieved profiles.

109        For this study, we used a 14-channel Humidity and Temperature Profiling (HATPRO)  
110        microwave radiometer (Rose et al. 2005). This is a fourth-generation system, which is part of  
111        the Collaborative Lower Atmospheric Mobile Profiling System (CLAMPS; Wagner et al. 2019).  
112        The instrument specifications are given in Table 1. The radiometric uncertainty in these  
113        observations were determined via a time-series analysis of the observed brightness  
114        temperatures when the atmosphere could be assumed to be quasi-stationary. These values are  
115        provided in Table 1. These radiometric uncertainties are assumed to be uncorrelated between  
116        the different channels.

117        **2.2. AERI**

118        The second passive remote sensor studied here is the Atmospheric Emitted Radiance  
119        Interferometer (AERI). The AERI is a Fourier transform spectrometer designed to measure  
120        infrared radiation emitted by the atmosphere between 3.3 and 19  $\mu\text{m}$  in wavelength (3000 to  
121        520  $\text{cm}^{-1}$ ) with a spectral resolution of 0.5  $\text{cm}^{-1}$ . The AERI was designed specifically for the  
122        Department of Energy’s Atmospheric Radiation Measurement (ARM) program (Turner et al.  
123        2016a; Knuteson et al. 2004 a,b). Its specifications can also be found in Table 1.

124        The radiometric uncertainty in the AERI observations is derived from the imaginary  
125        component of the AERI’s calibration equation (Revercomb et al. 1988), and thus the noise  
126        spectrum can be derived for each sky observation period. Turner and Blumberg (2019) have  
127        demonstrated that the radiometric noise in the AERI observations is spectrally uncorrelated.  
128

129        **2.3. NCAR water vapor DIAL**

130        Water vapor differential absorption lidar (DIAL) work by transmitting pulsed laser energy at  
131        two wavelengths, one of which is selected to have markedly higher water vapor absorption  
132        than the other. These two frequencies are typically referred to as the on-line and off-line

133 frequencies. If the two wavelengths are spectrally close to each other (e.g., within a nm in  
134 wavelength), then many of the terms that describe the ratio of the strength of the  
135 backscattered signals cancel out. The ratio of the on- to off-line return signals is directly related  
136 to the water vapor concentration profile.

137 The National Center for Atmospheric Research (NCAR) has developed a micropulse water  
138 vapor DIAL. The approach used by this lidar is the so-called "narrowband DIAL" approach  
139 wherein the laser emits monochromatic pulses of energy. Thus, because the characteristics of  
140 the absorption line are well known, the method is self-calibrating and no external calibration  
141 source is needed. Narrowband DIAL systems require extremely high spectral purity in the  
142 outgoing laser, as subtle changes in the wavelength (especially for the on-line channel) even for  
143 a small number of laser pulses in the averaging window can introduce biases in the derived  
144 water vapor profile because the incorrect absorption cross-section is used in the derivation.

145 The laser in the NCAR DIAL, henceforth called the nDIAL, emits low pulse energies at high  
146 pulse repetition rate (Spuler et al 2015). The outgoing laser beam is expanded by a portion of  
147 the primary telescope, which makes the lidar system eye-safe. The nDIAL system has its origins  
148 at Montana State University (MSU), wherein commercially available laser diodes developed for  
149 telecommunications were used as the laser source (Nehrir et al. 2012), and MSU continues to  
150 collaborate with NCAR to advance the nDIAL technology. A single photon counting detector is  
151 used to detect the backscattered signals in both the on-line and off-line channels. High  
152 transmission, narrowband interference filters are used to reject energy (e.g., solar background)  
153 outside the desired frequency range of the desired signals. The technical details of this system  
154 are provided in Table 1.

155 The signal-to-noise ratio (SNR) in DIAL systems is strongly dependent upon the strength of  
156 the backscattering signal as a function of range. Aerosol particles provide an efficient scattering  
157 source, and because aerosol concentration decreases markedly above the top of the PBL, the  
158 SNR also drops sharply above this level. However, the actual range wherein the lidar makes  
159 good water vapor measurements is a function of the pulse energy, the efficiency of the  
160 detector system (e.g., size of the telescope, transmission of the detection optics, sensitivity of  
161 the detector), and the vertical profiles of both the aerosol and water vapor concentrations. For  
162 this study, the backscattered photon data were coadded for 1-minute before deriving the water  
163 vapor profile.

164 Virtually all lidar systems have difficulties accurately measuring atmospheric properties  
165 close to the lidar itself. Ultimately, this is due to a mismatch between the outgoing laser beam  
166 and the detector and leads to a systematic error that varies with height. This systematic error  
167 reduces to zero at some range, and the region where the error is nonzero is referred to as the  
168 "overlap" region. For many lidar systems, an empirically determined correction can be applied  
169 to reduce the maximum range of the non-zero overlap error. For the current version of the  
170 nDIAL, approximately the lowest 500 m suffers from a varying overlap correction (S. Spuler,  
171 personal communication), and thus is not used in this analysis.

172 The uncertainty in the nDIAL observations is directly calculated by assuming that the  
173 detected backscatter signal follows a Poisson distribution, and propagating the uncertainty in  
174 the backscatter profile through the DIAL equation. A similar approach was used for the SGP  
175 Raman lidar, and the noise estimate derived from Poisson statistics agrees with that derived  
176 using an autocovariance analysis (Turner et al. 2014).

177 The nDIAL has been deployed in a number of different field campaigns. In particular, the  
178 water vapor profile observed by the nDIAL have been compared to water vapor profiles  
179 measured by radiosondes and independently retrieved from collocated AERI and MWR systems  
180 (Weckwerth et al. 2016). These comparisons demonstrate that the nDIAL agrees well with these  
181 other sensors (e.g., the bias error relative to radiosondes is less than 0.3 g/m<sup>3</sup>) and has no  
182 significant day vs. night differences in sensitivity (e.g, due to solar background). In 2018, NCAR  
183 constructed 4 additional units (bringing the total number of nDIAL systems to five), which were  
184 deployed in a network configuration at the Department of Energy's Atmospheric Radiation  
185 Measurement (ARM) Southern Great Plains site (SGP, Sisterson et al. 2016) from April through  
186 July 2019.  
187

#### 188 **2.4. Vaisala water vapor DIAL**

189 Vaisala is also developing a micropulse water vapor DIAL (henceforth called the vDIAL). This  
190 lidar system is based upon the CL51 ceilometer design; this ceilometer is used operationally  
191 around the world. Unlike the nDIAL, the vDIAL transmits a spectrally broad pulse of laser  
192 energy that encompasses several water vapor absorption lines ("on-line channel") and in a  
193 nearby spectral window with no absorption lines ("off-line"). This approach is less technically  
194 demanding on the laser specifications (e.g., the requirement for high spectral purity is much  
195 smaller), but the tradeoff is that the measurement is no longer self-calibrating (Newsom et al.  
196 2020). For this particular broadband DIAL implementation, the reference measurement is a  
197 well-calibrated surface level in-situ sensor integrated into the DIAL, and measurements from  
198 this sensor are used in an iterative retrieval approach to derive the water vapor profile  
199 (Newsom et al. 2020).

200 The vDIAL actually consists of two independent broadband DIAL systems integrated  
201 together. The first system has a wide field-of-view, thereby resulting in a very small overlap  
202 region and allowing the lidar to profile water vapor down to 50 m above ground level (AGL).  
203 However, this wide field-of-view results in additional solar background photons and the SNR  
204 decreases very rapidly with range. The second system has a much narrower field of view, which  
205 results in a deeper overlap region but also enables the lidar to profile water vapor much higher.  
206 Cross-talk between the two independent systems is eliminated by operating one system for 5-s,  
207 and then operating the other for the next 5-s. The water vapor profiles are derived  
208 independently for the wide and narrow field-of-view systems, and then they are merged  
209 linearly between 300 and 400 m. Additional details on this system are provided in Newsom et  
210 al. (2020).

211 The vDIAL system uses analog detection, and thus the uncertainties in the backscatter do  
212 not follow a Poisson distribution like in the nDIAL. Instead, the uncertainties in the vDIAL water  
213 vapor profile are estimated by deriving water vapor profiles every 2-minutes, and computing  
214 the standard deviation from these data at each height across a 20-minute window to provide  
215 the uncertainty in the standard 20-min average water vapor profile.

216 The vDIAL system was deployed to the ARM SGP in May-June 2017, where it was compared  
217 against water vapor profiles observed by the ARM Raman lidar (Turner et al. 2016b; Turner and  
218 Goldsmith 1999), radiosondes, and retrieved from the AERI.

219 **3. Retrieval algorithm**

220 Passive spectral radiometers, such as the MWRs and AERIs, measure radiance, and  
 221 thermodynamic profiles must be retrieved from these observations. However, this is an ill-  
 222 posed problem, as there could exist multiple solutions (e.g., different thermodynamic profiles)  
 223 that would yield the observed radiance. Thus, the retrieval algorithm must incorporate  
 224 additional information to constrain the solution to a potentially valid solution. Here, we have  
 225 elected to use the optimal estimation approach (Rodgers 2000; Maahn et al. 2020), which is a  
 226 1-dimensional variational method. We have modified the AERIoe optimal estimation retrieval  
 227 algorithm (Turner and Löhnert 2014) to use AERI and/or MWR data, together with *a priori*  
 228 dataset that specifies how temperature and humidity covary with height, as input. This  
 229 algorithm has already been modified to include additional observations, such as water vapor  
 230 lidars (Turner and Blumberg 2019), and thus in these cases the retrieval is finding the  
 231 temperature and humidity profiles that satisfies both the observed radiance and the (partial)  
 232 profile of water vapor observed by the DIAL simultaneously.

233 We desire to retrieve the thermodynamic profile  $X$  (i.e., both the temperature and  
 234 humidity profile, so  $X = [T_1, T_2, \dots, T_p]^T, [q_1, q_2, \dots, q_p]^T$  where  $T_i$  and  $q_i$  are the temperature  
 235 and water vapor mixing ratio in the  $i^{\text{th}}$  vertical bin. We will refer to  $X_n$  as the state vector on  
 236 the  $n^{\text{th}}$  iteration. The observations from the AERI, MWR, and DIALs will form the observation  
 237 vector  $Y$ . A forward model  $F$  is used to compute a pseudo observation  $F(X)$ , which is then  
 238 compared with  $Y$ . If they disagree, then the state vector is modified to provide a new estimate  
 239 ( $X_{n+1}$ ) following

$$240 \quad X_{n+1} = X_a + (\gamma S_a^{-1} + K_n^T S_\epsilon^{-1} K_n)^{-1} K_n^T S_\epsilon^{-1} (Y - F(X_n) + K_n(X_n - X_a)) \quad (\text{Eq 1})$$

241 where  $K$  is the Jacobian of  $F$ ,  $X_a$  is the mean *a priori*, and  $S_a$  is the covariance matrix of the *a*  
 242 *priori* dataset (see Section 3.2).  $S_\epsilon$  denotes the combined forward model and observation error  
 243 covariance matrix. The observation error for the single instruments is considered as described  
 244 in the subsection of Section 2 and the forward model uncertainty is discussed in Section 3.1.  
 245 The superscripts  $T$  and  $^{-1}$  denote matrix transpose and matrix inverse, respectively. Because  $F$  is  
 246 moderately non-linear in  $X$ , optimal estimation is formulated as an iterative method, where the  
 247 subscript  $n$  indicates the iteration number; for our studies, we typically start with  $X_0 = X_a$ . The  
 248 scalar  $\gamma$  is used to stabilize the retrieval when  $n$  is small to improve the convergence rate and  
 249 decreases to unity as  $n$  increases; the description on how  $\gamma$  is used is explained in Turner and  
 250 Löhnert (2014). Note that due to the non-linearity of the forward models applied for the  
 251 microwave and infrared radiative transfer, the Jacobians are required to be recomputed for  
 252 each iteration. We continue to iterate Eq 1 until

$$253 \quad (F(X_{n+1}) - F(X_n))^T (K_n S_a K_n^T + S_\epsilon)^{-1} (F(X_{n+1}) - F(X_n)) \ll m \quad (\text{Eq 2})$$

254 where  $m$  is the dimension of  $Y$ .

255        **3.1. Forward models**

256        As shown by Eq 1, a forward model is needed to transform the current state vector  $X_n$  into  
257        the observational domain so it can then be compared to the observation vector  $Y$ . In this  
258        study, four different forward models are used (one for each instrument).

259        For the passive radiometers, the forward models are line-by-line radiative transfer models.  
260        The monochromatic MonoRTM radiative transfer model (Clough et al. 2005; Payne et al. 2011)  
261        is used to simulate MWR observations, and the line-by-line radiative transfer model LBLRTM  
262        (Clough et al. 1995; Mlawer and Turner 2016) is used to simulate the AERI. In the latter, the  
263        monochromatic spectra are convolved with a tophat function in the time domain and then  
264        transformed to the spectral domain via a Fourier transform; this applies the AERI's lineshape  
265        function to the calculation. The vertical grid used in these calculations is specified by the *a*  
266        *priori* data. The pressure profile is computed from the temperature and humidity data from the  
267        current state vector using the hypsometric equation. The spectral regions used in the retrieval  
268        are given in Table 1. In the infrared, many trace gases have absorption bands, and while the  
269        spectral regions used in the retrieval are primarily sensitive to water vapor and carbon dioxide  
270        (where the latter provides the sensitivity to temperature), there are minor contributions to the  
271        downwelling radiance by other gases. We utilize the US Standard Atmosphere to provide  
272        profiles of these other trace gases for this study, but our results are insensitive to this choice.

273        To incorporate the DIAL data into the Eq 1, a forward model is needed for each lidar also.  
274        The purest forward model would simulate the profiles of backscatter energy that would be  
275        observed in both the on- and off-line channels for a given water vapor profile. We could have  
276        also used the profile of differential optical depth between range bins as our observation.  
277        However, we have elected to use the derived water vapor concentration from each lidar in the  
278        observation vector. This results in a trivial forward model for each lidar: essentially, the  
279        forward model just converts water vapor mixing ratio to water vapor number concentration for  
280        the nDIAL. The output of the vDIAL is water vapor mixing ratio, so that forward model is just  
281        the unity function.

Deleted: W

282        **3.2. The *a priori* dataset**

283        There has been only one campaign that had an AERI, HATPRO, and water vapor DIAL  
284        collocated with each other: the Perdigao campaign that was held in Portugal from 1 May to 15  
285        June 2017 (Fernando et al. 2019). We specified a 48-level vertical grid for the retrievals,  
286        starting at 0 m above ground level (AGL), the next level at 10 m AGL, and each subsequent  
287        height bin is 10% thicker than the previous one. Although  $\sim$ 150 radiosondes were launched  
288        during Perdigao, these are not enough to accurately compute the level-to-level covariance for  
289        the 96-element state vector (i.e.,  $X$  has 48 levels for temperature, and 48 for water vapor).  
290        Therefore, we used 1571 radiosondes launched in the months of April, May, June, and July over  
291        the last decade by the Portuguese weather service at Lisbon to compute  $X_a$  and  $S_a$ . This *a*  
292        *priori* information was used in all of the retrievals shown here.

293        The vDIAL was not part of the Perdigao deployment, so we are using AERI and vDIAL data  
294        collected between 15 May to 12 June 2017 at the SGP site instead. Both the Perdigao and SGP  
295        datasets used here were collected in the spring, but the SGP climatology is different than that in  
296        Portugal necessitating the use of a different *a priori* dataset. We have used over 2000

298 radiosondes launched at the SGP during the months of April, May, and June over the past  
299 decade to derive the *a priori* information for this site.

300 **3.3. Characterizing the information content in the retrieved profile**

301 One advantage of the optimal estimation framework is that the uncertainties in the  
302 retrieval, which includes contributions from both the uncertainties in the observations and *a*  
303 *priori* as well as the sensitivity of the forward model, is a direct output of the framework. If the  
304 "optimal" solution is  $X_{op}$ , which is the solution after both  $\gamma = 1$  and Eq 2 indicates that the  
305 solution has converged after  $nc$  iterations, then the covariance of the optimal solution is given  
306 by

$$S_{op} = (S_a^{-1} + K_{nc}^T S_e^{-1} K_{nc})^{-1} \quad (\text{Eq 3})$$

307 We will look at the square root of the diagonal elements of  $S_{op}$  to quantify how the 1- $\sigma$   
308 uncertainties of the retrieved profiles change as different instrument combinations are used in  
309 the observation vector.

310 A second advantage of this method is that the averaging kernel  $A$  provides a direct estimate  
311 of the sensitivity of the retrieved profile at each height to perturbations at that height. This  
312 matrix is computed as

$$A = (S_a^{-1} + K_{nc}^T S_e^{-1} K_{nc})^{-1} K_{nc}^T S_e^{-1} K_{nc} = I - S_{op} S_a^{-1} \quad (\text{Eq 4})$$

313 The diagonal components of  $A$  provides the degrees of freedom for signal (DFS; Rodgers 2000)  
314 for each height in the retrieved profile. If the observations had very high information content  
315 at each level of the retrieved profile, then the diagonal elements of  $S_{op}$  would be small relative  
316 to the diagonal elements of the *a priori*, and thus the trace of  $A$  would approach the dimension  
317 of  $X$ . The total DFS, which is equal to the trace of  $A$ , provides a metric for how many  
318 independent pieces of information exist in the observation.

319 For this study, we recognize that the matrices  $A$ ,  $S_{op}$ , and  $S_a$  really have four equal sized  
320 quadrants that correspond to

$$\begin{bmatrix} (T, T) & (T, q) \\ (q, T) & (q, q) \end{bmatrix}$$

321 We will look at the portions of  $A$  and  $S_{op}$  that correspond to  $(T, T)$  and  $(q, q)$  independently.  
322 Furthermore, as we will see, the DFS is typically much smaller than unity, so we will look at the  
323 profile of the cumulative DFS (cDFS), as this allows us to quickly determine how many  
324 independent levels are below some specified height, which is advantageous when talking about  
325 where in the vertical the different instruments provide sensitivity to changes in temperature  
326 and water vapor.

327 We want to highlight that even though lidars make explicitly range resolved measurements,  
328 their information content in the derived water vapor profile is not the same as the number of  
329 range bins. The actual information content at height  $z$  depends strongly on the noise level of  
330 the observation there. Even direct derivations of water vapor from lidar signals would benefit  
331 from being cast into a retrieval framework like what we've specified in Eq 1 because then the *a*  
332 *priori* information could be used to constrain the derived water vapor when the instrument's  
333 SNR decreases (e.g., Sica and Haefele 2016).

337 **4. Results**

338 Several studies have demonstrated that ground-based thermodynamic retrievals in the PBL  
339 using only AERI observations have 2-4 times larger total DFS in both temperature and water  
340 vapor than retrievals that use only microwave data (Löhnert et al. 2009; Blumberg et al. 2015;  
341 Wulfmeyer et al 2015). However, what is not known is how the information content changes  
342 when partial profiles of water vapor from a differential absorption lidar (since the DIAL  
343 observations extend only from the top of the region where full overlap is achieved to a height  
344 where its SNR becomes small) are included in a retrieval considering the synergy of AERI, MWR,  
345 and nDIAL or vDIAL. For example, does including a partial water vapor profile in the retrieval  
346 result in AERI+DIAL and MWR+DIAL having equivalent cDFS for water vapor? Does including a  
347 partial water vapor profile in a simultaneous retrieval of  $T(z)$  and  $q(z)$  (as we are doing here in  
348 Eq 1) improve the temperature profile in any way?

349 In order to answer these questions, we performed eight sets of retrievals using data from  
350 the Perdigao field campaign in Portugal (Table 2): four were using passive-only measurements  
351 (MWRz, MWRzo, AERI, and AERI+MWRz), and four included the nDIAL together with those  
352 passive measurements. “MWRz” denotes the case when only zenith-pointing MWR brightness  
353 temperature observations were used in the retrieval, whereas “MWRzo” denotes the case where  
354 both zenith and off-zenith (i.e., “oblique” elevation scans) are used. Crewell and Löhnert (2007)  
355 demonstrated that adding elevation scan observations at frequencies where the atmosphere is  
356 optically thick, and assuming horizontal homogeneity of the PBL, resulted in a marked increase  
357 in the information content and hence accuracy of the retrieved temperature profile. However,  
358 only observations made at frequencies above 55 GHz are used in these elevation scans. Even at  
359 low elevation angles, frequencies channels below 55 GHz are too transparent and thus the  
360 assumption of horizontal homogeneity fails very frequently (Crewell and Löhnert 2007).

361 As the vDIAL will soon be the first commercially available DIAL instrument for water vapor  
362 profiling (H. Winston, personal communication), a major objective is to evaluate how including  
363 this lidar dataset with passive observations changes the information content in the retrieved  
364 profiles. In addition, we show the impact of the vDIAL relative to the nDIAL on our retrievals.  
365 However, vDIAL (ARM SGP) and nDIAL (Perdigao) observations are only available at different  
366 locations with different *a priori* datasets. In order to overcome this issue, the comparisons were  
367 carried out in relation to the AERI instruments, which operated at both sites. The comparison of  
368 the AERI-only from ARM-SGP and Perdigao allows us to characterize the impact of the prior on  
369 the retrievals, since the two AERI instruments deployed in Portugal and at the SGP site have  
370 similar error characteristics (not shown). Ultimately, we have looked at the differences  
371 between the AERI-only and AERI+xDIAL retrievals (where x is either “v” or “n”) at the two sites.

372 **4.1. Case study example**

373 To illustrate the differences between the various passive-only and passive+active retrievals,  
374 we selected a case during Perdigao on 15 May 2017 at 05:07 UTC. This is a clear sky event, and  
375 is representative of the retrieval quality during the entire field campaign. Figure 1 shows the  
376 retrieved temperature (panel A) and water vapor mixing ratio (WVMR, panel B), and the  
377 associated  $1-\sigma$  uncertainties of each (panels C and D, respectively) derived from the square root  
378 of the diagonal of the retrieval error covariance  $S_{op}$ . The black line in panels A and B denote

379 the coincident radiosonde, whereas the other colors denote the different passive-only  
380 retrievals.

381 All three passive-only retrievals (MWRzo, AERI, and AERI+MWRzo) identify the surface-  
382 based inversion, although the retrievals that include the AERI capture it more accurately (Fig  
383 1A). Furthermore, the retrievals that include the AERI are able to better match the radiosonde  
384 temperature observations above 1.5 km, whereas the MWRzo retrieval is showing a bias at  
385 those altitudes. None of the three retrievals are able to capture the small-scale variability in the  
386 vertical observed by the radiosonde due to the relatively coarse vertical resolution of the  
387 retrievals. The uncertainties in the MWRzo temperature retrievals are about 50% larger (or  
388 more) over the lowest 3 km relative to the AERI retrievals (Fig 1C), which agrees qualitatively  
389 with the differences to the radiosonde seen in Fig 1A.

390 The water vapor retrievals (Fig 1B) show two basic vertical patterns: the MWRzo retrieval is  
391 markedly drier than the radiosonde below 1 km, whereas the AERI and AERI+MWRzo retrieval  
392 starts dry, then becomes too wet (between 500 and 1000 m), and then becomes drier than the  
393 radiosonde above 1500 m. Interestingly, the nDIAL water vapor profile is also drier than the  
394 radiosonde below 1500 m, and agrees better with the MWRzo profile. However, the retrievals  
395 that use the AERI data have markedly smaller uncertainties than the MWRzo below 1.5 km;  
396 above that height, the uncertainty in the MWRzo is smaller than the AERI, although the  
397 AERI+MWRzo retrieval has the smallest uncertainties over the entire lowest 3 km as would be  
398 expected for a variational retrieval method.

399 Including the nDIAL data above 500 m into the retrieval, and thus finding a solution that  
400 simultaneously fits both the observed radiance and the partial WVVMR profile of the DIAL within  
401 their uncertainties, yields the results shown in Fig 2. The largest impact, not surprisingly, is on  
402 the retrieved water vapor profile (Fig 2B). The inclusion of the nDIAL data forces the retrievals  
403 that also include the AERI to reduce the amount of water vapor between 500 and 1000 m  
404 (where the AERI-based retrievals were too wet in Fig 1B), which has the impact of increasing  
405 the amount of water vapor in the AERI retrievals below 500 m (Fig 2B), resulting in the  
406 AERI+nDIAL and AERI+MWRzo+nDIAL agreeing much better with the radiosonde. Between 800  
407 and 1500 m, the MWR+nDIAL retrieved profile is essentially the same as the nDIAL profile,  
408 suggesting that the MWR is not adding any significant information to the DIAL's observation.  
409 The impact of the nDIAL data on the water vapor uncertainty profiles can clearly be seen in Fig  
410 2D, where all retrievals have the similar uncertainty above about 800 m where the DIAL data  
411 are being used. Including the DIAL data into the retrievals has a minor impact on the retrieved  
412 temperature profiles, as all three seem to agree a bit better qualitatively with the radiosonde  
413 above 1000 m (comparing Fig 2A with Fig 1A), and the 1- $\sigma$  uncertainties in temperature are  
414 slightly smaller (Fig 2C with Fig 1C).

#### 415 **4.2. Comparing mean uncertainty profiles**

416 While the case study above may be representative, the quality of a retrieval (i.e., its  
417 uncertainty and information content) is case specific. To provide a more complete picture of  
418 how the different passive-only and active+passive retrievals compare, we computed the mean  
419 1- $\sigma$  uncertainty profiles from all of the retrievals performed during Perdigao, as a wide range of  
420 environmental conditions (e.g., the surface temperature ranged from approximately 9 to 33 °C  
421 and the precipitable water vapor from 1.1 to 3.1 cm) were observed during the 5-week

422 campaign. Figure 3 shows these mean uncertainty profiles for temperature (left) and water  
423 vapor (right) for the different passive-only (solid lines) and active+passive (broken lines), and  
424 Table 2 provides the mean values at 3 different heights.

425 Considering the passive-only retrievals, combining the AERI and MWR together has little  
426 impact on the resulting temperature retrieval in the lowest 3 km or on the water vapor retrieval  
427 below 1.5 km, compared to the AERI-only retrieval. However, the MWRz and MWRzo  
428 outperform the AERI for water vapor above 2 km. Most strikingly, the benefit of the passive  
429 retrieval synergy can be seen for water vapor above 1.5 km, where the improvement is up to  
430 30% compared to the single sensor retrievals. Adding the elevation scanning data to the MWR  
431 retrieval (i.e., the MWRzo vs MWRz) results in a smaller uncertainty in the temperature profile,  
432 especially below 400 m.

433 Including the nDIAL data into the retrievals greatly reduces the  $1-\sigma$  uncertainty in the water  
434 vapor profiles for all active+passive retrievals (relative to the passive-only results), and results  
435 in a slight decrease in the temperature uncertainty also. [The addition of the nDIAL data to](#)  
436 [either the MWR- or AERI-based retrievals results in smaller uncertainties in water vapor than](#)  
437 [either the lidar by itself \(dotted black line\) or the passive-only retrievals \(Fig 3 right\).](#) The AERI-  
438 based retrievals show smaller uncertainties than the MWR-based retrievals, with the exception  
439 in the water vapor retrievals above 2 km where the MWR-based retrieval has a smaller  
440 uncertainty than the AERI retrieval. The uncertainty in the AERI+nDIAL water vapor retrieval  
441 between 500 m and 2 km, where the nDIAL data are used, is slightly smaller than the  
442 uncertainty in the MWRz+nDIAL retrieval, suggesting that the AERI is adding more information  
443 to the DIAL observations than the MWR. However, above 2 km the combination of all sensors  
444 has distinguishably the best performance, indicating that all instruments are contributing to the  
445 sensor synergy. In quantitative numbers, the WVMR can be retrieved via sensor synergy with  
446 accuracies between 0.4 and 0.6 g kg<sup>-1</sup> in the lowest 3 km, which between 1 and 2 km (the region  
447 where DIAL shows its optimal performance), is an uncertainty reduction of up to 50% compared  
448 to the passive retrieval synergy.

449

### 450 4.3. Comparing bias profiles

← Formatted: Heading 2, Indent: First line: 0"

451 Figure 4 shows the bias profiles in temperature and humidity relative to radiosondes  
452 launched during Perdigao. The radiosondes were launched within 100 m of the remote  
453 sensors, and 169 individual comparisons are included in these bias profiles.

454 The temperature bias profiles (Fig 4, left) demonstrate that the retrievals that include AERI  
455 data have markedly smaller biases than the retrievals that did not. The inclusion of the nDIAL  
456 observations with the AERI (i.e., AERI+nDIAL, AERI+MWRz+nDIAL) did not markedly change the  
457 bias relative to the AERI-only and AERI+MWRz. However, for the retrievals that uses the MWR  
458 data and not the AERI, the inclusion of the nDIAL data did result in smaller temperature biases  
459 above approximately 1 km.

460 The water vapor mixing ratio bias profiles (Fig 4, right) illustrate the MWRz-only and MWRe-  
461 only profiles had markedly larger magnitudes than the retrievals that included AERI data.  
462 Including nDIAL data into these MWR-based retrievals (i.e., the MWRz+nDIAL and  
463 MWRe+nDIAL) resulted in smaller mixing ratio biases above 500 m (recall the nDIAL data below  
464 500 m were not used in this analysis due to known systematic issues), but that the water vapor

465 bias below 600 m was largely unchanged. Similarly, including the nDIAL data into the AERI-  
466 based retrievals also reduced the size of the water vapor bias above 1 km, although the impact  
467 of this additional dataset was smaller because the accuracy in the water vapor retrievals above  
468 1 km is better for AERI-only retrievals relative to MWRz-only and MWRe-only retrievals.  
469

#### 470 **4.4. Comparing mean cDFS profiles**

471 The optimal estimation framework used in this study uses the *a priori* to help constrain the  
472 ill-posed retrieval, thereby allowing the algorithm to converge to a realistic solution more  
473 frequently. Looking at the DFS profile, especially when summed with altitude from the surface  
474 (called here the cumulative DFS profile), enables one to understand where the independent  
475 data in the observations are located vertically. Figure 5 shows the mean cumulative DFS  
476 profiles for the different retrievals; mean values at three specific heights are provided in Table  
477 3.

478 There are several important features in this figure. First, adding the elevation scanning data  
479 to the MWR retrieval (i.e., comparing the MWRz-only vs. MWRzo-only) increases the total DFS  
480 for temperature at 3 km by 0.4 (from 2.15 to 2.57), with almost all of this increase in the first  
481 500 m. [Note, however, that we have only used a single elevation angle to the MWRzo (Table  
482 1), and the inclusions of additional elevation angles would result in a slight increase the cDFS for  
483 temperature.] The AERI-only temperature retrieval has more information (3.87) in the lowest  
484 500 m than the MWRzo-only retrieval has in the lowest 3 km (2.57). Most of the information in  
485 the temperature retrievals is below 1.5 km, as the cDFS profiles become relatively constant  
486 above that level; this suggests that these passive-only and active+passive temperature  
487 retrievals will have limited ability to retrieve the structure of the temperature profile above  
488 that height.

489 The passive-only retrievals of water vapor show less total DFS (using the value at 3 km  
490 height) during Perdigao relative to datasets at other field campaigns (e.g., Turner and Löhner  
491 2014; Blumberg et al. 2015). This is likely due to the spread in the covariance of the prior,  
492 because if the prior had (hypothetically) negligible spread then the derived information content  
493 from the observations would be vanishingly small. Nonetheless, we can still use this prior to  
494 demonstrate how the addition of the DIAL data to the retrievals changes the information  
495 content. The cDFS profiles for the water vapor retrievals clearly show the impact of including  
496 the nDIAL data above 500 m, as the cDFS profiles for the active+passive retrievals are markedly  
497 larger above that height than the passive-only retrievals (i.e., with values between 6 to 7  
498 compared to 2 to 3 at 3 km). The additional information on water vapor in the AERI below 500  
499 m relative to the MWR is clearly seen. However, the lidar does not always provide data to the  
500 same altitude and its noise levels can depend on atmospheric conditions (e.g., if there is a cloud  
501 above the lidar or not), and thus the spread in the cumulative DFS profiles was quite large (e.g.,  
502 from 2.0 to 9.4 for the MWRz+nDIAL at 3 km height; Table 3).

#### 503 **4.5. Impact of clouds**

504 One of the often-stated advantages of MWR-based retrievals, relative to infrared-based  
505 retrievals, is the ability to profile through clouds because the optical thickness of the cloud is  
506 markedly smaller in the microwave relative to the infrared for a given liquid water path (LWP).

Deleted: 4

508 Figure 6 shows cDFS profiles from the MWRz-only and AERI-only temperature and water vapor  
509 retrievals during a 2h period when the sky transitioned from virtually clear sky to overcast.  
510 Three profiles with different LWP amounts (2, 10, and 60 g m<sup>-2</sup>, where the infrared is essentially  
511 opaque for the last – Turner 2007) are shown. The cloud base was at 1100 m and was assumed  
512 to be 100 m thick (there was no way to determine cloud top from other observations at the  
513 site). First, notice that as the cloud becomes optically thicker, the retrievals have more  
514 information about the temperature at cloud base. Second, the cloud becomes opaque in the  
515 infrared quickly, hence the cumulative DFS profile becomes essentially constant (especially for  
516 water vapor) above the cloud as the LWP values approach 60 g m<sup>-2</sup>. Meanwhile, the cloud is  
517 semi-transparent in the microwave for all LWP values, which is seen by the increasing cDFS  
518 profile (especially for water vapor) above the cloud. However, there is still only a small amount  
519 of information in the observations at heights above 1 km in the MWR (see left-hand panel of Fig  
520 5), and thus the increase in the information content in the MWR retrieval above the cloud is  
521 relatively limited.

Deleted: 5

522 The accurate understanding of where the information exists vertically is useful in order to  
523 properly assimilate these profiles into a numerical weather prediction model. There is often  
524 significant level-to-level correlation in the uncertainties of profiles retrieved from passive  
525 remote sensors (e.g., see Figure 10 of Turner and Blumberg 2019), and most data assimilation  
526 systems are not yet configured to handle correlated error in the observations. Coniglio et al.  
527 (2019) used the cDFS profile to identify the heights that should be assimilated to minimize the  
528 amount of correlated error from the retrieved profiles. Starting at a specified height (e.g., 50  
529 m), they identified heights where the cDFS had increased by 1 above that height, and this  
530 process continued until they either were unable to identify any other points or had reached the  
531 maximum height that they wanted to assimilate. This is illustrated by the dots on the profiles in  
532 Fig 6, with the first height taken at 50 m. For the AERI-retrieved profiles, three levels would be  
533 assimilated below the cloud with an additional level at cloud base or just above; the height of  
534 all of the temperature levels is pretty consistent for these three profiles. For the MWR, only  
535 two levels would be assimilated due to the lower information content in the microwave  
536 observations, with the height of the second point changing dramatically due to how the cloud  
537 influences the vertical distribution of the DFS profile. Again, we remind the reader that the  
538 total DFS seen in this example is lower than that seen using this same retrieval framework in  
539 other field campaigns; we attribute this to the lack of spread in the *a priori* dataset used at  
540 Perdigao.

Deleted: 4

#### 541 4.6. Sensitivity to the nDIAL vs. vDIAL

542 The impact of adding any new observation depends partially on its error covariance matrix,  
543 as observations with larger uncertainties will add less information to the retrieved profile than  
544 observations with smaller uncertainties. For many lidars, coadding photon counting data in  
545 either time or altitude reduces the random errors, and thus would increase the information  
546 content and impact of using these lidar data in retrievals such as these. However, other  
547 features of the observations are also important. For example, during Perdigao, the lowest  
548 range gate that was considered useful from the nDIAL was at 500 m; data below that level  
549 suffered from systematic errors associated with the overlap function of the lidar (S. Spuler,  
550 personal communication). However, the vDIAL was designed to make good measurements at

554 50 m above the surface, although generally speaking its maximum range is much less (order 1  
555 km; Newsom et al. 2020) than the nDIAL system (which frequently makes good water vapor  
556 measurements to altitudes well above 2 km). A natural question is how would the results  
557 already shown change if the vDIAL system was used instead of the nDIAL?

558 Unfortunately, this isn't straight-forward to answer as the vDIAL was not collocated with the  
559 other Perdigao instruments. Instead, we use the 6-week deployment of the vDIAL at the ARM  
560 SGP site (Newsom et al. 2020), which has an AERI with similar noise characteristics as the AERI  
561 deployed at Perdigao, as a surrogate. However, different *a priori* datasets were used for the  
562 retrievals at the two sites, which impacts the retrievals and hence the analysis. To help adjust  
563 for the contribution of the two priors, we performed AERI-only retrievals and AERI+vDIAL  
564 retrievals at the SGP so that we could look at the difference between the two, and compare  
565 that to the difference between the AERI-only and AERI+nDIAL retrievals at Perdigao (Figure 7).

566 The impact of the vDIAL data on the water vapor retrieval is most significant between 300  
567 and 1500 m and reaches relative values of up to 50% uncertainty reduction compared to the  
568 AERI-only retrieval. Above 1500 m, the AERI+vDIAL WVMR uncertainties increase quickly with  
569 height and approach the AERI-only uncertainties at 3 km. The AERI+nDIAL uncertainties are  
570 very similar to the AERI-only below 500 m (because the nDIAL data is not available at those  
571 levels), but are approximately 2x smaller than the AERI-only for all height between 500 m and 3  
572 km. Further, the change in the cDFS between 500 m and 3 km is larger for the nDIAL system  
573 relative to the vDIAL (Table 3). Thus, the ability of the nDIAL to see deeper into the troposphere  
574 than the vDIAL is clearly shown. Interestingly, the water vapor uncertainty in the AERI+vDIAL is  
575 smaller than the AERI+nDIAL in the 500 to 900 m range; however, this could easily be changed  
576 by adjusting how the DIAL data were coadded in the nDIAL (which had 1-min temporal  
577 resolution relative to the 20-min temporal resolution of the vDIAL – see Table 1).

578 Perhaps most noteworthy is the relative impact of the two DIALs on the retrieved  
579 temperature profile. The addition of the vDIAL data has almost no impact on the uncertainty or  
580 the cDFS profile relative to the AERI-only (Fig. 7, Tables 2 and 3), whereas the nDIAL has a  
581 marked impact on the retrieved temperature profile in the range from 500 m to 2.5 km with an  
582 reduction of the uncertainty of up to 0.25 K compared to the AERI-only retrieval. Here, the  
583 instrument synergy is obtained through a more exact determination of the water vapor profile  
584 by the nDIAL, which enables the AERI to reach a higher DFS value for temperature.

## 585 5. Conclusions

586 Many applications require profiles of temperature and humidity in the PBL. However, the  
587 accuracy and information content from different ground-based remote sensing instruments is  
588 not the same. Previous work (e.g., Löhnert et al. 2009; Blumberg et al. 2015) demonstrated  
589 that there is more information content in both temperature and water vapor from spectral  
590 infrared measurements (such as made by the AERI) than in spectral microwave radiometer  
591 measurements. These results depend strongly on the characteristics of the instrument systems  
592 being used; for example, if future generation MWRs are improved to have smaller random  
593 errors, then the information content in the observations would increase. The on-line python  
594 modules provided by Maahn et al. (2020) can be used to explore how the information content  
595 would change for different assumed random error levels in the MWR.

Deleted: 6

Deleted: 6

598 This study investigated the impact of ground-based sensor synergy for PBL thermodynamic  
599 profiling, and in particular, how the information content and random errors would change if an  
600 active remote sensor such as a water vapor DIAL was included into the retrieval. An open  
601 question going into this research was whether the inclusion of the water vapor DIAL  
602 observations with MWR radiance observations would have the same information content as  
603 retrievals that used the DIAL with the AERI observations. An important aspect of this study is  
604 that the same *a priori* data and retrieval framework were used for all of the different retrievals  
605 shown in this paper, which is crucial to truly quantify the differences as different retrieval  
606 frameworks can result in markedly different retrievals (Maahn et al. 2020). Furthermore, the  
607 2017 NASA Decadal Survey recommended an increased focus on thermodynamic profiling of  
608 the atmospheric boundary layer from space (National Academies 2018), and coupling passive  
609 microwave and infrared with active DIAL remote sensing is one possible solution. We have  
610 shown that including the DIAL data increases the water vapor information content and reduces  
611 water vapor errors in both the AERI+DIAL and MWR+DIAL retrievals, relative to the passive-only  
612 retrievals. However, the AERI+DIAL continues to have more information on water vapor than  
613 the MWR+DIAL. The best retrieval performance is observed when all three instruments are  
614 combined in one retrieval. Improvements are shown that decrease the uncertainty by 50%  
615 compared to passive-only retrievals between 1 and 2 km. At Perdigao, the AERI is shown to  
616 dominate retrieval accuracy in the lowest 500 m, from 500 m to 2 km it is the DIAL that  
617 primarily determines the accuracy, and above 2 km the three instruments complement each  
618 other optimally to obtain the best solution. Furthermore, the addition of the water vapor DIAL  
619 observations (slightly) improves the information content in temperature retrievals from the  
620 AERI+DIAL, but has no impact on the temperature profiles for the MWR+DIAL.

621 Passive ground-based remote sensors are relatively common, as these technologies are  
622 more mature, have been commercially available for several decades, and have been operated  
623 in networks (e.g., Caumont et al. 2016; Geerts et al. 2017; Yang and Min 2018). The recent  
624 advances in water vapor DIAL (e.g., Spuler et al. 2015; Newsom et al. 2020) are leading to the  
625 possibility that the two DIALs used in this study could be commercially available in the next  
626 several years, which is why they formed the focus of this study. There are other  
627 thermodynamic profiling active remote sensors that could be combined with MWRs and AERIs:  
628 for example, Raman lidar and Radio Acoustic Sounding Systems (RASS). Studies have been  
629 conducted combining Raman lidar with both MWR data (e.g., Barrera-Verdejo et al 2016; Foth  
630 and Pospichal 2017) and AERI data (e.g., Turner and Blumberg 2019); however, these studies  
631 were in different environments using different *a priori* datasets, which makes quantitatively  
632 comparing their accuracy and information content problematic. There are currently efforts  
633 underway to evaluate the impact of RASS virtual temperature profile observations on both AERI  
634 and MWR observations. Developing improved synergistic retrievals and sensor synergy are the  
635 goals of many groups, including the PROfiling of the atmospheric Boundary layer at European  
636 scale (PROBE; Cimini et al. 2020).

637 Sensor synergy does not have to just involve ground-based sensors. Ground-based MWR  
638 and AERI observations can also be combined with satellite observations to improve information  
639 content and accuracy, especially in the middle- and upper troposphere. Feltz et al. (2003)  
640 showed the impact on AERI retrievals and how these improved profiles could be used for  
641 evaluating thermodynamic structure near storms, while Ebelt et al. (2013) performed a more

Deleted: s

643 classical information content study. Additional efforts (e.g., such as Toprov and Löhnert 2020)  
644 are needed, which show the impact of the high-temporal and high-spectral resolution  
645 geostationary infrared sounders with ground-based remote sensing systems and the impact on  
646 stability indices and other parameters.

647 It is possible that readers will consider this study as a suggestion about the optimal ground-  
648 based solution for thermodynamic profiling, especially for future operational networks. This  
649 paper provides insights into only one aspect of the cost-benefit solution (i.e., the relative  
650 differences of information content); considerations as to ease of use, durability and hardiness,  
651 calibration stability, and other scientific traits (e.g., does the instrument provide information on  
652 macro- or microphysical cloud properties, aerosol properties, trace gases, etc.) also need to be  
653 considered.

654

## 655 Acknowledgments

656 This research was supported in part by the Department of Energy's Atmospheric System  
657 Research (ASR) program (DE-SC0014375 and 89243019SSC000034) and NOAA's Atmospheric  
658 Science for Renewable Energy program. We thank the groups that helped to collect the two  
659 primary datasets from the Perdigao field campaign in used in this paper: Petra Klein, Elizabeth  
660 Smith, Josh Gebauer, and Tyler Bell at the University of Oklahoma; and Scott Spuler, Matt  
661 Hayman, and Tammy Weckwerth at the National Center for Atmospheric Research.  
662 Additionally, we thank Raisa Lehtinen, Reijo Roininen, and Christoph Münkel at Vaisala and Rob  
663 Newsom at Pacific Northwest National Laboratory for the collection of the DIAL dataset at the  
664 SGP site. This article supports activities associated with COST (European Cooperation in Science  
665 and Technology) Action CA18235 "PROBE" (<http://www.probe-cost.eu>). We would like to  
666 thank Jason English for constructive comments on an earlier version of this manuscript. This  
667 paper does not imply endorsement for any particular instrument, nor reflect the views or  
668 official position of NOAA or the U.S. government.

## 669 References

670 Barrera-Verdejo, M., S. Crewell, U. Löhnert, E. Orlandi, and P. Di Girolamo, 2016: Ground-based  
671 lidar and microwave radiometry synergy for high vertical resolution absolute humidity  
672 profiling. *Atmos. Meas. Techniq.*, **9**, 4013-4028, doi:10.5194/amt-9-4013-2016.  
673 Bluestein, H.B., Z.B. Wienthoff, D.D. Turner, D.W. Reif, J.C. Snyder, K.J. Thiem, and J.B. Houser,  
674 2017: A comparison of the fine-scale structures of a prefrontal wind-shift line and a  
675 strong cold front in the Southern Plains of the U.S. *Mon. Wea. Rev.*, **145**, 3307-3330,  
676 doi:10.1175/MWR-D-16-0403.1.  
677 Blumberg, W.G., D.D. Tuner, U Löhnert, and S. Castleberry, 2015: Ground based temperature  
678 and humidity profiling using spectral infrared and microwave observations. Part II:  
679 Actual retrieval performance in clear-sky and cloudy conditions. *J. Appl. Meteor.*  
680 *Climatol.*, **54**, 2305 – 2319.  
681 Caumont, O., D. Cimini, U. Löhnert, L. Alados-Arboledas, R. Bleisch, F. Buffa, M.E. Ferrario, A.  
682 Haefele, T. Huet, F. Madonna, and G. Pace, 2016: Assimilation of humidity and

683 temperature observations retrieved from ground-based microwave radiometers into a  
684 convective-scale NWP model. *Q. J. Roy. Meteor. Soc.*, doi:10.1002/qj.2860.

685 Cimini, D., E. Campos, R. Ware, S. Albers, G. Giuliani, J. Oreamuno, P. Joe, S.E. Koch, S. Cober,  
686 and E. Westwater, 2011: Thermodynamic atmospheric profiling during the 2010 winter  
687 Olympics using ground-based microwave radiometry. *IEEE Trans. Geosci. Remote Sens.*,  
688 49, 4959-4969, doi:10.1109/TGRS.2011.2154337.

689 Cimini, D., M. Nelson, J. Guldner, and R. Ware, 2015: Forecast indices from a ground-based  
690 microwave radiometer for operational meteorology. *Atmos. Meas. Tech.*, 8, 315-333,  
691 doi:10.5194/amt-8-315-2015.

692 Cimini, D., P.W. Rosenkranz, M.Y. Tretyakov, M.A. Koshelev, and F. Ramano, 2018: Uncertainty  
693 of atmospheric absorption model: Impact on ground-based radiometer simulations and  
694 retrievals. *Atmos. Chem. Phys.*, 18, 15231-15259, doi:10.5194/acp-18-15231-2018.

695 [Cimini, D., M. Haeffelin, S. Kotthaus, U. Löhner, P. Martinet, E. O'Connor, C. Walden, M. Coen, and J. Preissler, 2020: Towards the profiling of the atmospheric boundary layer at European scale— introducing the COST action PROBE. Bull. Atmos. Sci. Tech.](#), 1, 23-42,  
696 doi:10.1007/s42865-020-00003-8.

697 Clough, S.A., M.W. Shephard, E.J. Mlawer, J.S. Delamere, M.J. Iacono, K. Cady-Pereira, S.  
698 Boukabara, and P.D. Brown, 2005: Atmospheric radiative transfer modeling: A summary  
699 of the AER codes. *J. Quant. Spectroc. Radiative Trans.*, 91, 233-244,  
700 doi:10.1016/j.jqsrt.2004.05.058.

701 Coniglio, M.C., G.S. Romine, D.D. Turner, and R.D. Torn, 2019: Impacts of targeted AERI and  
702 Doppler lidar wind retrievals on short-term forecasts of the initiation and early evolution  
703 of thunderstorms. *Month. Wea. Rev.*, 147, 1149-1170, doi:10.1175/MWR-D-0351.1

704 Crewell, S., and U. Löhner, 2007: Accuracy of boundary layer temperature profiles retrieved  
705 with multi-frequency, multi-angle microwave radiometry, *IEEE Trans. Geosci. Remote  
706 Sens.*, 45(7), 2195-2201.

707 Dabberdt, W.F., and coauthors, 2005: Multifunction mesoscale observing networks. *Bull. Amer.  
708 Meteor. Soc.*, 86, 961-982, doi:10.1175/BAMS-86-7-961.

709 De Angelis, F., D. Cimini, U. Löhner, O. Caumont, A. Haeffele, B. Pospichal, P. Martinet, F. Navas-  
710 Guzman, H. Klein-Baltink, J.-C. Dupont, and J. Hocking, 2017: Long-term observations minus  
711 background monitoring of ground-based brightness temperatures from a microwave  
712 radiometer network. *Atmos. Meas. Tech.*, 10, 3947-3961, doi:10.5194/amt-10-3947-2017.

713 Degelia, S.K., X. Wang, and D.J. Stensrud, 2019: An evaluation of the impact of assimilating AERI  
714 retrievals, kinematic profilers, rawinsondes, and surface observations on a forecast of  
715 nocturnal convection initiation event during the PECAN field campaign. *Month. Wea.  
716 Rev.*, in press.

717 Ebell, K., E. Orlandi, A. Hünerbein, U. Löhner, and S. Crewell, 2013: Combining ground-based  
718 with satellite-based measurements in the atmospheric state retrieval: Assessment of  
719 the information content, *J. Geophys. Res. Atmos.*, 118, 6940-6956,  
720 doi:10.1002/jgrd.50548.

721 Feltz, W. F., W.L. Smith, H.B. Howell, R.O. Knuteson, H. Woolf, and H.E. Revercomb, 2003: Near-  
722 continuous profiling of temperature, moisture, and atmospheric stability using the  
723 Atmospheric Emitted Radiance Interferometer (AERI). *J. Appl. Meteor.*, 42, 584-597.

724

725

726 Fernando, H.J., and 48 coauthors (including D.D. Turner), 2019: The Perdigao: Peering into  
 727 microscale details of mountain winds. *Bull. Amer. Meteor. Soc.*, **100**, 799-819,  
 728 doi:10.1175/BAMS-D-17-0227.1.

729 Foth, A., and B. Pospichal, 2017: Optimal estimation of water vapour profiles using a  
 730 combination of Raman lidar and microwave radiometer. *Atmos. Meas. Tech.*, **10**, 3325-  
 731 3344, doi:10.5194/amt-10-3325-2017.

732 Geerts, B., and coauthors, 2017: The 2015 Plains Elevated Convection At Night field project.  
 733 *Bull. Amer. Meteor. Soc.*, **98**, 767 – 786.

734 Grasmick, C., B. Geerts, D.D. Turner, Z. Wang, and T.M. Weckwerth, 2018: The relation between  
 735 nocturnal MCS evolution and its outflow boundaries in the stable boundary layer: An  
 736 observational study of the 15 July 2015 MCS in PECAN. *Month. Wea. Review*, **146**, 3203-  
 737 3226, doi:10.1175/MWR-D-18-0169.1

738 Hu, J., N. Yussouf, D.D. Turner, T.A. Jones, and X. Wang, 2019: Impact of ground-based remote  
 739 sensing boundary layer observations on short-term probabilistic forecasts of a tornadic  
 740 supercell event. *Wea. Forecasting*, **34**, 1453-1476, doi:10.1175/WAF-D-18-0200.1.

741 Johnson, A., X. Wang, K. Hagh, and D.B. Parsons, 2018: Evaluation of forecasts of a convectively  
 742 generated bore using an intensively observed case study from PECAN. *Month. Wea.  
 743 Rev.*, **146**, 3097-3122, doi:10.1175/MWR-D-18-0059.1

744 Knuteson, R. O., and coauthors, 2004a: Atmospheric Emitted Radiance Interferometer. Part I:  
 745 Instrument design. *J. Atmos. Oceanic Technol.*, **21**, 1763-1776.

746 Knuteson, R. O., and coauthors, 2004b: Atmospheric Emitted Radiance Interferometer. Part II:  
 747 Instrument performance. *J. Atmos. Oceanic Technol.*, **21**, 1777-1789.

748 Loveless, D.M., T.J. Wagner, D.D. Turner, S.A. Ackerman, and W.F. Feltz, 2019: A composite  
 749 perspective on bore passages during the PECAN campaign. *Month. Wea. Rev.*, **147**,  
 750 1395-1413, doi:10.1175/MWR-D-18-0291.1.

751 Löhner, U., D.D. Turner, and S. Crewell, 2009: Ground-based temperature and humidity  
 752 profiling using spectral infrared and microwave observations. Part 1: Simulated retrieval  
 753 performance in clear sky conditions. *J. Appl. Meteor. Clim.*, **48**, 1017-1032,  
 754 doi:10.1175/2008JAMC2060.1

755 Löhner, U., and O. Maier, 2012: Operational profiling of temperature using ground-based  
 756 microwave radiometry at Payerne: Prospects and challenges. *Atmos. Meas. Techniq.*, **5**,  
 757 1121-1134, doi:10.5194/amt-5-1121-2012.

758 Maahn, M., D.D. Turner, U. Loehnert, D.J. Posselt, K. Ebelt, G.G. Mace, and J.M. Comstock,  
 759 2020: Optimal estimation retrievals and their uncertainties: What every atmospheric  
 760 scientist should know. *Bull. Amer. Meteor. Soc.*, **101**, E1512-1523, doi:10.1175/BAMS-D-  
 761 19-0027.1.

762 Mlawer, E.J., and D.D. Turner, 2016: Spectral radiation measurements and analysis in the ARM  
 763 program. *The Atmospheric Radiation Measurement Program: The First 20 Years.*  
 764 Meteor. Monograph, 57, Amer. Meteor. Soc., 14.1-14.17,  
 765 doi:10.1175/AMSMONOGRAPHS-D-15-0027.1

766 Mueller, D., B. Geerts, Z. Wang, M. Deng, and C. Grasmick, 2017: Evolution and vertical  
 767 structure of an undular bore observed on 20 June 2015 during PECAN. *Month. Wea.  
 768 Rev.*, **145**, 3375-3794, doi:10.1175/MWR-D-16-0305.1

769 National Academies, 2018: Thriving on our changing planet: A decadal strategy for Earth

Deleted: R

Deleted: accepted

772 observation from space. National Academies Press, doi:10.17226/24938, available from  
773 <http://nap.edu/24938>.

774 National Research Council (NRC) Committee on Developing Mesoscale Meteorological  
775 Observational Capabilities to Meet Multiple National Needs, 2009: Observing Weather  
776 and Climate from the Ground Up: A Nationwide Network of Networks. National  
777 Academies Press, 234 pp.

778 Nehrir, A.R., K.S. Rapasky, and J.L. Carlsten, 2012: Micropulse water vapor differential  
779 absorption lidar: Transmitter design and performance. *Opt. Express*, 20, 137-151.

780 Newsom, R.K., D.D. Turner, R. Lehtinen, C. Muenkel, J. Kallio, and R. Roininen, 2020: Evaluation  
781 of a compact broadband differential absorption lidar for routine water vapor profiling in  
782 the atmospheric boundary layer. *J. Atmos. Oceanic Technol.*, 37, 47-65,  
783 doi:10.1175/JTECH-D-18-0102.1.

784 Payne, V.H., E.J. Mlawer, K.E. Cady-Pereira, and J.-L. Moncet, 2011: Water vapor continuum  
785 absorption in the microwave. *IEEE Trans. Geosci. Remote Sens.*, 49, 2194-2208,  
786 doi:10.1109/TGRS.2010.2091416.

787 Revercomb, H.E., H. Buijs, H.B. Howell, D.D. LaPorte, W.L. Smith, and L.A. Sromovsky, 1988:  
788 Radiometric calibration of IR Fourier transform spectrometers: Solution to a problem  
789 with the high-resolution interferometer sounder. *Appl. Opt.*, 27, 3210-3218.

790 Rodgers, C.D., 2000: *Inverse Methods for Atmospheric Sounding: Theory and Practice*. Series on  
791 Atmospheric, Oceanic, and Planetary Physics, Vol. 2, World Scientific, 238 pp.

792 Rose, T., S. Crewell, U. Löhnert, and C. Simmer, 2005: A network suitable microwave radiometer  
793 for operational monitoring of the cloudy atmosphere. *Atmos. Res.*, 75, 183-200,  
794 doi:10.1016/j.atmosres.2004.12.005.

795 Sica, R.J., and A. Haefele, 2016: Retrieval of water vapor mixing ratio from a multiple channel  
796 Raman-scatter lidar using an optimal estimation method. *Appl. Opt.*, 55, 763-777,  
797 doi:10.1364/AO.55.000763.

798 Sisterson, D.L, R.A. Peppler, T.S. Cress, P.J. Lamb, and D.D. Turner, 2016: The ARM Southern  
799 Great Plains (SGP) site. *The Atmospheric Radiation Measurement Program: The First 20*  
800 Years, Meteor. Monograph. Amer. Meteor. Soc. 57, 6.1-6.14,  
801 DOI:10.1175/AMSMONOGRAPH-D-16-0004.1.

802 Spuler, S. M., K.S. Repasky, B. Morley, D. Moen, M. Hayman, and A.R. Nehrir, 2015: Field-  
803 deployable diode-laser-based differential absorption lidar (DIAL) for profiling water  
804 vapor. *Atmos. Meas. Tech.* 8, 1073-1087, DOI:10.5194/AMT-8-1073-2015.

805 Toms, B.A, J.M. Tomaszewski, D.D. Turner, and S.E. Koch, 2017: Analysis of a lower-tropospheric  
806 gravity wave train using direct and remote sensing measurement systems. *Mon. Wea.*  
807 *Rev.*, 145, 2791-2812, doi:10.1175/MWR-D-0216.1.

808 Toporov, M., and U. Löhnert, 2020: Synergy of Satellite- and Ground-Based Observations for  
809 Continuous Monitoring of Atmospheric Stability, Liquid Water Path and Integrated  
810 Water Vapor, *J. Appl. Meteor. Climatol.*, early-online release,  
811 <https://doi.org/10.1175/JAMC-D-19-0169.1>

812 Turner, D.D., and J.E.M. Goldsmith, 1999: Twenty-Four-Hour Raman Lidar Water Vapor  
813 Measurements during the Atmospheric Radiation Measurement Program's 1996 and  
814 1997 Water Vapor Intensive Observation Periods. *J. Atmos. Oceanic Technol.* 16, 1062-  
815 1076.

816 Turner, D.D., 2007: Improved ground-based liquid water path retrievals using a combined  
817 infrared and microwave approach. *J. Geophys. Res.*, **112**, D15204,  
818 doi:10.1029/2007JD008530

819 Turner, D.D., R.O. Knuteson, H.E. Revercomb, C. Lo, and R.G. Dedecker, 2006: Noise reduction  
820 of Atmospheric Emitted Radiance Interferometer (AERI) observations using principal  
821 component analysis. *J. Atmos. Oceanic Technol.*, **23**, 1223-1238

822 Turner, D. D., and U. Löhnert 2014: Information content and uncertainties in thermodynamic  
823 profiles and liquid cloud properties retrieved from the ground-based Atmospheric  
824 Emitted Radiance Interferometer (AERI). *J. Appl. Meteor. Climatol.*, **53**, 752-771,  
825 doi:10.1175/JAMC-D-13-0126.1.

826 Turner, D.D., V. Wulfmeyer, L.K. Berg, and J.H. Schween, 2014: Water vapor turbulence profiles  
827 in stationary continental convective mixed layers. *J. Geophys. Res.* **119**, 1-15,  
828 DOI:10.1002/2014JD022202.

829 Turner, D.D., E.J. Mlawer, and H.E. Revercomb, 2016a: Water vapor observations in the ARM  
830 program. *The Atmospheric Radiation Measurement Program: The First 20 Years.*  
831 Meteor. Monograph, 57, Amer. Meteor. Soc., 13.1-13.18,  
832 doi:10.1175/AMSMONOGRAPH-D-15-0025.1

833 Turner, D.D., J.E.M. Goldsmith, and R.A. Ferrare, 2016b: Development and applications of the  
834 ARM Raman lidar. *The Atmospheric Radiation Measurement Program: The First 20*  
835 *Years*, Meteor. Monograph. Amer. Meteor. Soc. **57**, 18.1-18.15,  
836 DOI:10.1175/AMSMONOGRAPH-D-15-0026.1.

837 Turner, D.D., and W.G. Blumberg, 2019: Improvements to the AERloe thermodynamic profile  
838 retrieval algorithm. *IEEE Selected Topics Appl. Earth Obs. Remote Sens.*, **12**, 1339-1354,  
839 doi:10.1109/JSTARS.2018.2874968.

840 Wagner, T. J., W. F. Feltz, and S. A. Ackerman, 2008: The temporal evolution of convective  
841 indices in storm-producing environments. *Wea. Forecasting*, **23**, 786 – 794.

842 Wagner, T.J., P.M. Klein, and D.D. Turner, 2019: A new generation of ground-based mobile  
843 platforms for active and passive profiling of the boundary layer. *Bull. Amer. Meteor.*  
844 *Soc.*, **100**, 137-153, doi:10.1175/BAMS-D-17-0165.1.

845 Weckwerth, T.M., K. Weber, D.D. Turner, and S.M. Spuler, 2016: Validation of a new water  
846 vapor micropulse differential absorption lidar (DIAL). *J. Atmos. Oceanic Technol.* **33**,  
847 2353-2372, DOI:10.1175/JTECH-D-16-0119.1.

848 Wulfmeyer, V., R.M. Hardesty, D.D. Turner, A. Behrendt, M. Cadeddu, P. Di Girolamo, P.  
849 Schluessel, J. van Baelen, and F. Zus, 2015: A review of the remote sensing of lower-  
850 tropospheric thermodynamic profiles and its indispensable role for the understanding  
851 and simulation of water and energy cycles. *Rev. Geophys.*, **53**, 819-895,  
852 doi:10.1002/2014RG000476

853 Yang, J., and Q. Min, 2018: Retrieval of atmospheric profiles in the New York State Mesonet  
854 using one-dimensional variational algorithm. *J. Geophys. Res.*, doi:  
855 10.1029/2018JD028272

856

857

858

859

860

**Table 1:**  
Important specifications of the instruments used in this paper

Instrument	Specifications
MWR (HATPRO G4)	<ul style="list-style-type: none"> <li>• 7 frequencies between 22.2 and 31.4 GHz</li> <li>• 7 frequencies between 51.2 and 58.0 GHz</li> <li>• Off-zenith data collected at elevations of 18° and 162°</li> <li>• 1-s sky average, with elevation scans performed every 5 min; retrieval used single spectrum (both zenith and off-zenith) at desired time (e.g., close to sonde launch time)</li> <li>• Reference: Rose et al. 2005</li> </ul>
AERI	<ul style="list-style-type: none"> <li>• 324 wavenumbers in these intervals: 612-618, 624-660, 674-713, 713-722, 538-588, 860.1-864.0, 872.2-877.5, 898.2-905.4 <math>\text{cm}^{-1}</math></li> <li>• 15-s sky average every 30-s; retrieval used single spectrum at desired time (e.g., close to sonde launch time)</li> <li>• Principal component noise filter used to reduce random error (Turner et al. 2006)</li> <li>• Reference: Knuteson et al. 2004 a,b</li> </ul>
nDIAL	<ul style="list-style-type: none"> <li>• Narrowband DIAL, transmitting at 830 nm</li> <li>• Temporal resolution: 1-min</li> <li>• Vertical resolution: 75-m</li> <li>• Minimum height: 500 m; Maximum height was approx. 3 km (typical)</li> <li>• Telescope receiver area (far field): 935 <math>\text{cm}^2</math></li> <li>• Average transmitted pulse power: 5 <math>\mu\text{J}</math> pulses at 9 kHz (45 mW)</li> <li>• Reference: Spuler et al. 2015; Weckwerth et al. 2016</li> </ul>
vDIAL	<ul style="list-style-type: none"> <li>• Broadband DIAL, transmitting at 911 nm</li> <li>• Temporal resolution: 20-min</li> <li>• Vertical resolution: variable from 100 m at 100 m AGL to 200 m at 1 km</li> <li>• Minimum height: 50 m; Maximum height was approx. 1 km (typical)</li> <li>• Telescope receiver area (far field): 615 <math>\text{cm}^2</math></li> <li>• Average transmitted pulse power: 5.5 <math>\mu\text{J}</math> pulses at 8 kHz (44 mW)</li> <li>• Reference: Newsom et al. 2020</li> </ul>

861

862

863

864  
865  
866  
867  
868  
869

**Table 2:** Average uncertainty values (derived from  $S_{op}$ ) at three levels for temperature and humidity for the different instrument combinations used in this study. The passive-only retrievals are highlighted in gray, whereas the active+passive are in white. The values in parentheses at 3 km show the 10<sup>th</sup> and 90<sup>th</sup> percentile at that height, thereby providing a measure of the amount of variability in these statistics for each retrieval.

	Temperature Uncertainty [°C]			Water Vapor Uncertainty [g kg <sup>-1</sup> ]		
	500 m	1000 m	3000 m	500 m	1000 m	3000 m
MWRz-only	1.1	1.6	1.4 (1.3,1.4)	1.1	1.4	0.9 (0.8,0.9)
MWRzo-only	1.1	1.5	1.4 (1.3,1.4)	1.1	1.3	0.9 (0.8,0.9)
AERI-only	0.6	0.9	1.0 (0.9,1.2)	0.7	1.0	1.0 (0.8,1.1)
AERI+MWRz	0.6	0.9	0.9 (0.8,1.3)	0.7	1.0	0.7 (0.6,0.8)
MWRz+nDIAL	1.0	1.4	1.3 (1.3,1.4)	0.7	0.7	0.7 (0.5,0.9)
MWRzo+nDIAL	1.0	1.3	1.3 (1.3,1.4)	0.7	0.7	0.7 (0.5,0.8)
AERI+nDIAL	0.5	0.8	0.9 (0.8,1.2)	0.6	0.6	0.7 (0.5,1.1)
AERI+MWRz+nDIAL	0.5	0.8	0.9 (0.8,1.2)	0.6	0.6	0.6 (0.4,0.8)
AERI-only (SGP)	0.4	0.6	1.0 (0.8,1.4)	0.7	1.0	1.8 (0.9,1.5)
AERI+vDIAL (SGP)	0.4	0.6	1.0 (0.8,1.4)	0.4	0.7	1.1 (0.8,1.4)

870  
871  
872  
873  
874  
875  
876  
877  
878  
879  
880

**Table 3:** Average cDFS values at three levels for temperature and humidity for the different instrument combinations used in this study. The passive-only retrievals are highlighted in gray, whereas the active+passive are in white. The values in parentheses at 3 km show the 10<sup>th</sup> and 90<sup>th</sup> percentile at that height, thereby providing a measure of the amount of variability in these statistics for each retrieval.

	Temperature cDFS value [unitless]			Water vapor cDFS value [unitless]		
	500 m	1000 m	3000 m	500 m	1000 m	3000 m
MWRz-only	1.5	1.8	2.2 (2.1,2.2)	0.9	1.1	1.9 (1.7,2.0)
MWRzo-only	1.9	2.2	2.6 (2.6,2.6)	0.9	1.1	1.9 (1.7,2.0)
AERI-only	3.9	4.6	5.5 (5.0,5.7)	1.5	1.8	2.7 (1.9,3.4)
AERI+MWRz	3.9	4.6	5.6 (5.2,5.7)	1.5	2.0	3.2 (2.7,3.8)
MWRz+nDIAL	1.5	1.8	2.2 (2.1,2.2)	1.1	2.6	6.2 (2.0,9.4)
MWRzo+nDIAL	1.8	2.2	2.6 (2.5,2.6)	1.1	2.6	6.2 (2.0,9.4)
AERI+nDIAL	3.9	4.5	5.5 (5.3,5.6)	1.7	3.3	7.0 (2.8,10.1)
AERI+MWRz+nDIAL	3.9	4.5	5.5 (5.3,5.6)	1.7	3.3	7.2 (3.2,10.2)
AERI-only (SGP)	4.8	5.5	6.6 (5.4,7.2)	1.7	2.1	3.0 (1.9,3.8)
AERI+vDIAL (SGP)	4.8	5.5	6.6 (5.5,7.1)	2.5	4.2	5.5 (2.4,8.4)

881  
882  
883

884 **Figures:**

885

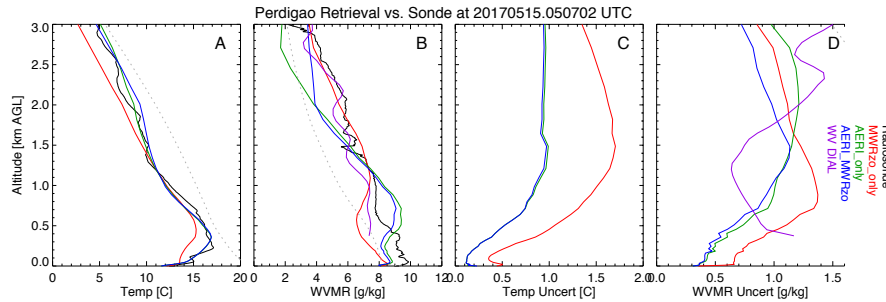


Fig 1: The retrieved profiles of temperature (A) and water vapor (B), with the uncertainties in these profiles (panels C and D, respectively), for the passive-only retrievals with the MWRzo only (red), AERI only (green), and AERI+MWRzo (blue) on 05:07 UTC on 15 May 2017 during Perdigao. The collocated radiosonde temperature and water vapor profiles are shown in black in (A) and (B), respectively. The water vapor observed by the DIAL and its uncertainty are included in the figure, although it is not used in any of these retrievals. The dotted black lines in A and B are the mean prior profiles.

886

887

888

889

890

891

892

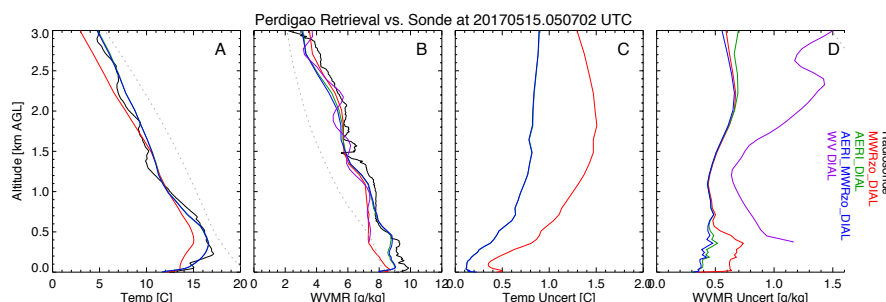


Fig 2: Same as Fig 1, except that the retrievals combine active and passive data with the MWRzo+DIAL (red), AERI+DIAL (green), and AERI+MWRzo+DIAL (blue). The water vapor observed by the DIAL and its uncertainty are included in the retrievals. See text for more details.

893

894  
895

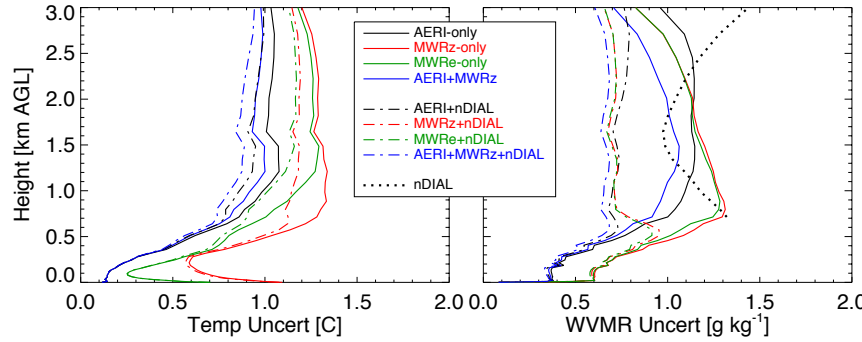


Fig 3: The mean uncertainty in temperature (left) and water vapor mixing ratio (right) for passive-only (solid lines) and active+passive (broken lines) retrievals during Perdigao. [The black dotted line is the mean uncertainty from the nDIAL.](#)

896  
897  
898  
899  
900  
901  
902  
903

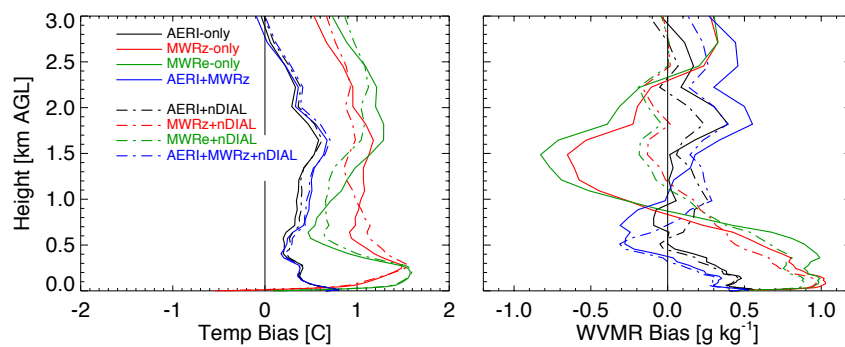


Fig 4: The bias in temperature (left) and water vapor mixing ratio (right) for passive-only (solid lines) and active+passive (broken lines) retrievals relative to radiosondes during Perdigao.

904

905  
906  
907  
908

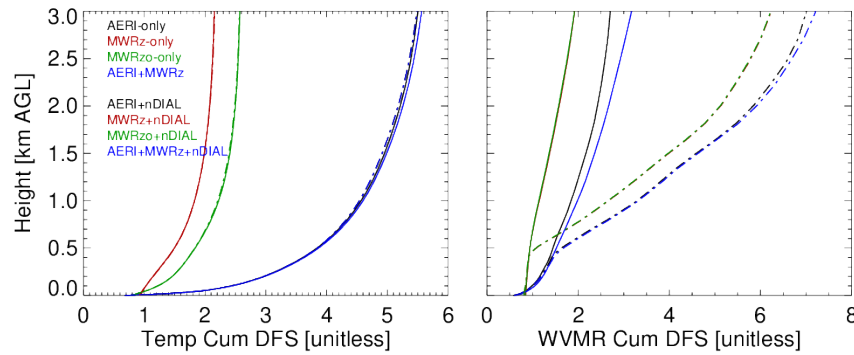


Fig 5: The mean cumulative degrees of DFS for temperature (left) and water vapor mixing ratio (right) for passive-only (solid lines) and active+passive (broken lines) retrievals during Perdigao. Note that the water vapor cumulative DFS profiles for MWRz and MWRzo retrievals are virtually identical (see Table 3) and hence overlap.

Deleted: 4

909  
910  
911  
912  
913

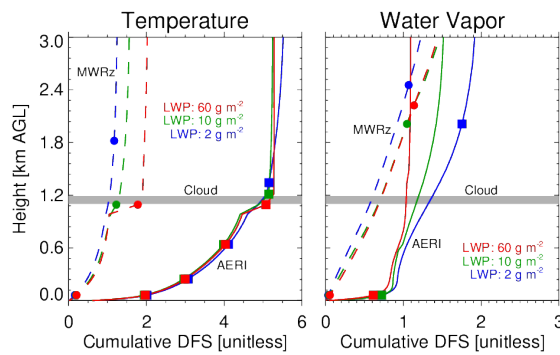


Fig 6: Profiles of cumulative degrees of freedom of signal from MWRz-only (dashed curves with dots) and AERI-only (solid curves with squares) temperature (left) and water vapor (right) retrievals for three samples between 03:00 and 05:00 UTC on 27 May 2017 during Perdigao. The different colors correspond to different LWP path values in the overhead cloud, whose height is indicated with the horizontal gray bar. The solid symbols indicate

Deleted: 5

heights that would be assimilated, if the first level started at 50 m AGL and each level was separated by a unit of DFS. See the text for more details.

916  
917  
918

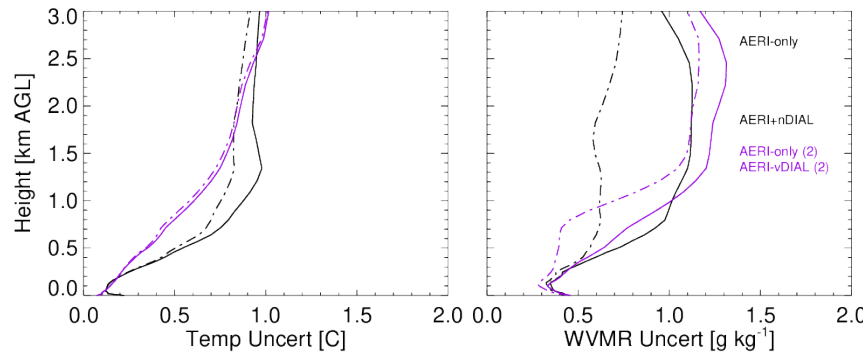


Fig 7: The mean uncertainty in temperature (left) and water vapor mixing ratio (right) for AERI-only (solid lines) and AERI+xDIAL (broken lines) retrievals during Perdigao (black) and SGP (purple), where the former used nDIAL data and the latter used vDIAL data. Note that different priors were used for the two locations; this impact is seen in the AERI-only retrievals as the noise levels of the two AERIs were similar.

Deleted: 6

919